Disentangling Interglacial Sea Level and Global Dynamic Topography: Analysis of Madagascar

S.N. Stephenson*[1], N. White*[1], T. Li[2,3] and L.F. Robinson[2]

[1]*Bullard Laboratories, Department of Earth Sciences, Madingley Rise, Madingley Road, University of Cambridge, Cambridge, CB3 0EZ, UK.*

[2]*School of Earth Sciences, University of Bristol, Wills Memorial Building, Queens Road, Bristol BS8 1RJ.*

[3]*Department of Earth and Planetary Sciences, Nanjing University, 163 Xianlin Road, Nanjing 210023, China.*

* *sns29@cam.ac.uk* * *njw10@cam.ac.uk*

Abstract

Global inventories of stable sea-level markers for the peak of the last interglacial period, Marine Isotopic Stage (MIS) 5e, play a pivotal role in determining sea-level changes and in testing models of glacial isostatic adjustment. Here, we present surveying and radiometric dating results for emergent terraces from northern Madagascar, which is generally regarded as a stable equatorial site. Fossil coral specimens were dated using conventional and open-system corrected uranium series methods. Elevation of the upper (undated) terrace decreases from 33.8 m to 29.5 m over a distance of 35 km. An intermediate terrace has an average radiometric age of 130.7 ± 13.2 ka (i.e. MIS 5e). Its elevation decreases from 9.3 m to 2.8 m over a distance of 80 km. The record of the lower terrace is fragmentary and consists of beach rock containing rare corals with ages of 1.6–3.8 ka. The spatial gradient of the MIS 5e marker is inconsistent with glacio-isostatic adjustment calculations. Instead, we propose that variable elevations of this marker around Madagascar, and possibly throughout the Indian Ocean, at least partly reflect spatial patterns of dynamic topography generated by sub-plate mantle convection.

1 Introduction

At active plate boundaries, vertical movements of the Earth's surface are dominated by interactions between quasi-rigid tectonic plates. In contrast, large tracts of plate interiors are regarded as relatively stable, which suggests that relative vertical displacements recorded along coastlines and islands require a different explanation. Since the 1990s, numerous studies have inferred that Quaternary uplift and subsidence of continental margins remote from active plate boundaries are predominantly caused by glacial isostatic adjustment (*Farrell and Clark*, 1976; *Mitrovica and Peltier*, 1991; *Mitrovica and Milne*, 2002). Thus, endemic Late Holocene sea-level highstands of $\sim$ 3 m within equatorial oceanic basins between 40° S and 40° N are accounted for by a distal phenomenon associated with melting icesheets, known as siphoning, which can produce relative (i.e. non-eustatic) sea-level falls during interglacial periods (*Mitrovica and Peltier*, 1991; *Milne et al.*, 2002). This phenomenon occurs when the flexural forebulge, that is located peripheral to the melting ice sheet, subsides. Since a significant part of this bulge can be submarine, its collapse triggers an increase in the volume of the oceanic basin that causes a relative sea level fall in equatorial regions. Siphoning is modulated by continental levering, which is caused by the flexural loading effect of rising sea level at continental margins (*Walcott*, 1972; *Nakada and Lambeck*, 1989; *Mitrovica and Milne*, 2002).

The last interglacial period, known as Marine Isotopic Stage (MIS) 5e, which lasted from 130–115 ka, is often exploited as an analogue for the present-day sea-level highstand. Oxygen isotopic records alone are unable to resolve ancient sea-level variations more accurately than ±12 m but they do suggest that MIS 5e sea level was similar to, or slightly higher than, present-day sea level (*Siddall et al.*, 2003; *Rohling et al.*, 2008). Probabilistic studies suggest that MIS 5e sea level peaked at 7.2 ± 1.3 m (e.g. *Kopp et al.*, 2009). An internally consistent database of U-Th radiometric ages of coral samples combined with isostatic modeling indicates that mean MIS 5e sea level peaked at 5.5–9.0 m (*Dutton and Lambeck*, 2012). Notwithstanding these globally averaged values, heights of MIS 5e sea-level markers along continental margins vary between 2.5 m and at least 25 m (*Blanchon et al.*, 2009; *Guiraud et al.*, 2010; *O'Leary et al.*, 2013; *Dutton et al.*, 2015). Several studies suggest that eustatic sea level may have fluctuated during the course of MIS 5e and a 3–6 m increase in sea level immediately after 120 ka has been proposed (e.g. *Blanchon et al.*, 2009; *O'Leary et al.*, 2013).

A significant complication is that the present-day elevation of ancient sea-level markers is expected to be at least partly controlled by the pattern of dynamic topography generated by sub-plate mantle convection (*Rovere et al.*, 2014; *Austermann et al.*, 2017). Residual depth observations from fringing coastlines of the South Atlantic Ocean show that dynamic topography varies by up to ± 1 km on length scales of $O(10^3)$ km (*Hoggard et al.*, 2016). Significantly, stratigraphic evidence suggests that observed dynamic topography grows and decays on million year timescales at rates of $O(10^{-1})$ mm yr^{-1} (*Al-Hajri et al.*, 2009; *Hartley et al.*, 2011; *Czarnota et al.*, 2013). One problem is that these length scales and timescales overlap with those associated with glacio-isostatic adjustment. This difficulty has been addressed using two complementary approaches. One approach sidesteps the issue by identifying stable continental margins and oceanic islands that are ostensibly unaffected by dynamic topographic displacements (e.g. *Blanchon et al.*, 2009; *Dutton et al.*, 2015; *O'Leary et al.*, 2013). However, it is increasingly clear that tectonically stable locations are a rare exception on Earth (*Hoggard et al.*, 2016). A second approach exploits numerical models of glacio-eustasy and of mantle flow as a means of dissecting competing influences (e.g. *Austermann et al.*, 2017).

Here, we take an alternative approach, which focuses on detailed examination of relative sea-level markers within equatorial oceanic basins that are often deemed tectonically stable. A key example is Madagascar whose northern and southern coastlines are rimmed by Quaternary reef deposits (Figure 1; *Battistini*, 1965). This island is regarded as tectonically stable after having rifted away from Africa and India in Cretaceous times and so it is usually included within databases of global sea-level markers used for glacial isostatic adjustment studies (e.g. *Pedoja et al.*, 2011; *Hibbert et al.*, 2016). Notwithstanding the pioneering geomorphic studies of *Battistini* (1965), the coastal deposits of Madagascar remain poorly studied with few reliable radiometric dates. Our principal goal is to present a suite of detailed field observations and radiometric dates from this significant equatorial site with a view to disentangling the competing influences of glacio-isostatic adjustment and dynamic topography.

2 Emergent Coral Reef Deposits

During a field campaign in October 2015, we mapped and surveyed emergent marine terraces that rim the northern Malagasy coastline (Figure 1d). The distribution, morphology and sedimentary facies of these terraces were determined and their elevations above high tide were measured using differential global positioning system (D-GPS) surveying relative to a portable base station. This surveying was carried out using a Thales ProMark-3 system with a tripod-mounted base station and two hand-held roving receivers. D-GPS measurements have a conservative accuracy of ±0.1 m relative to the base station. The height difference between modern and ancient sea-level markers is measured to quantify changes in relative sea level. To determine this difference, we establish a datum against which to measure elevations of mapped geomorphic markers. To start with, the elevation of the mean high water springs datum is determined in two different ways. First, we survey the elevation of modern geomorphic markers such as the upper limit of tidal notches, the inner margins of wavecut platforms, and heights of encrusting marine organisms. Each of these observations can be used to estimate the height of the local mean high water springs datum (e.g. *Rovere et al.*, 2016). The variation in elevation of these geomorphic markers is typically ±0.5 m. Secondly, additional checks were made by measuring local sea level and the time of this measurement. These sea-level estimates were then compared with a global tidal model that was calibrated against a historical tidal gauge located at 12.27745° S, 49.28397° E near Antsiranana (formerly known as Diego Suarez) and against a modern tidal gauge located at 18.15360° S, 49.42810° E near Taomasina (see Admiralty Tide Tables of UK Hydrographic Office, `https://www.admiralty.co.uk/`). The root mean squared (rms) uncertainties in tidal measurements with respect to the tidal model are ±0.5 m. Taken together, both sets of measurements indicate that the mean high water springs datum can be estimated with an uncertainty of ±0.5 m.

The principal paleo sea-level marker exploited in this study is the maximum elevation of dated fossil corals upon ancient, emergent fringing reefs. Coral samples were collected from their growth position at the highest point of each terrace. Cleaned samples were screened for the presence of calcite using X-ray diffraction and samples with > 90% aragonite were radiometrically dated using the uranium-series technique at the University of Bristol (*Chen et al.*, 2015). Open-system corrections were subsequently applied using the method described by *Thompson et al.* (2003). Both open-system and conventional dates are reported here (Table 1; Supplementary Material). Since corals grow on fringing reef flats in water depths that are no greater than ~ 2 m below the mean low water springs datum, coral heights are corrected to this datum, assuming an uncertainty of ± 1 m for paleo water depth (*Dutton et al.*, 2015; *Rovere et al.*, 2016). There is an additional uncertainty of ± 0.5 m in correcting the datum from mean high water springs to mean low water springs because tidal range is likely to vary by this amount along the coastline in question (*Egbert and Erofeeva*, 2002). Here, all elevation measurements are reported with respect to the mean low water springs datum. Provided that these uncertainties are uncorrelated, they can be summed in quadrature to yield a combined uncertainty for the difference between modern and paleo sea-level estimates derived from coral elevations of ± 1.2 m. Additional observations, such as detailed sedimentary facies and precise heights of both high and mean tidal markers were made to corroborate this approach.

Spectacular terraces are observed at Cap d'Ambre on the northernmost tip of Madagascar (Figures 2a and 3). Here, three distinctive surfaces occur at heights of 33.8 m, 9.3 m and 2.8 m above the mean low water springs datum, respectively (*Battistini*, 1965). The two highest terraces are characterized by erosive bases and sandy, coral-rich carbonate caps. The upper terrace has a low relief surface with abundant corals on its upper surface, which is taken to represent the mean low water springs datum at time of reef formation. Cross-bedded and bioturbated sandstones containing coral rubble underlie this reef deposit. Coral samples from this upper terrace have suffered from too much recrystallization to be used for radiometric dating.

The intermediate terrace has a more complex morphology (Figure 3). At its base, a coral-poor, bioturbated and occasionally cross-bedded sandstone bench that is $\sim 6.8 \pm 1.2$ m above the mean low water springs datum abuts a seaward-sloping wavecut platform of volcanogenic sedimentary rock (Figure 3). Landward, this platform intersects a minor cliff with a prominent notch, the mid-point of which is 10.0 ± 1.1 m above the mean low water springs datum. Coral heads protrude from both bench and wavecut platform up to within 0.7 m of the height of the deepest part of this notch (Figure 3). We interpret the center of the notch as an indicator of mean sea level and the top surface envelope of the coral heads located on the reefal flat as an indicator of the mean low water springs datum at time of coral growth (Figure 3c; e.g. *Dutton et al.*, 2015; *Rovere et al.*, 2016). The bioturbated and coral-poor sandstone bench was deposited below the mean low water springs datum and probably represents back-reef sedimentary deposits upon which corals on the reefal flat grew. These self-consistent observations indicate a difference in height between modern and paleo sea-level markers of 9.3 ± 1.2 m for the intermediate terrace. Calculated elevations of the notch and of the wavecut platform together with their uncertainties are listed in the Supplementary Material. Coral samples from this intermediate terrace have corrected radiometric dates of 125.5 ± 1.8 ka and 121.8 ± 1.5 ka (Samples 1 and 2; Figure 2b, Table 1). The lower terrace has an elevation of 2.8 m above the mean low water springs datum and comprises indurated beach rock that unconformably overlies volcaniclastic turbiditic sedimentary rocks intruded by occasional basaltic dykes. This beach rock contains shell fragments and occasional coral debris. One coral (Sample 3) from this lower terrace has a conventional age of 3.8 ± 0.3 ka.

At Cap Miné, 35 km south south east of Cap d'Ambre, a morphologically similar upper terrace has an elevation of 29.5 m. The terrace consists of cross-bedded and bioturbated coarse sandstones that are ~ 10 m thick and contain corals. It overlies volcaniclastic basement and is itself overlain by compositionally mature, fine grained, cross bedded and quartz-rich sands that were probably deposited by aeolian action. The top 5–10 m of this deposit have been altered to red laterite. As before, the intermediate terrace has a bioturbated sandstone bench at 4.6 ± 1.2 m above mean low water springs from which coral heads protrude to a height of up to 6.6 ± 1.2 m above mean low water springs (Figure 2c). Coral heads sampled at an elevation of 6.4 m above the mean low water springs datum have corrected ages of 139.0 ± 5.3 ka and 136.9 ± 2.3 ka (Samples 4 and 5; Figure 2d). At Ankirikiriky Bay, which is 25 km further southeastward along the coast, the upper terrace is absent and the intermediate terrace is much lower. Here, the sandstone bench has a height of 3.0 ± 1.2 m and coral heads protrude to a height of 4.3 ± 1.2 m above the mean low water springs datum. A sample from the top of these coral heads has a corrected age of 129.4 ± 1.8 ka (Sample 6). At Irodo, which is 80 km southeast of Cap d'Ambre, only the intermediate terrace is observed. It consists of a gently sloping erosional wavecut platform that is fringed by corals, which crop out at 2.8 ± 1.2 m above the mean low water springs datum (Figure 2e). At this location, four coral samples yield corrected radiometric ages of 141.8 ± 1.9, 126.6 ± 2.0, 126.9 ± 1.8, and 128.3 ± 1.9 ka (Samples 7–10).

Our combined geologic and geochronologic observations demonstrate that three discrete marine highstands are recorded around the northern coast of Madagascar. The undated upper terrace probably represents an interglacial period that predates MIS 5e. Its elevation decreases from 33.8 m to 29.5 m over a distance of 35 km between Cap d'Ambre and Cap Miné. The intermediate and lower terraces have average ages of 130.7 ± 13.2 ka (2σ) and 1.6–3.8 ka, which correlate with the last interglacial period and the middle of the current interglacial period, respectively (i.e. MIS 5e and MIS 1). A striking feature of the intermediate MIS 5e terrace is its decrease in elevation from 9.3 m to 2.8 m over a distance of 80 km (Figure 4b). Height of the sandstone bench immediately beneath the top surface of this intermediate terrace decreases from 6.8 m to 3.3 m between Cap d'Ambre and Ankirikiriky Bay (Figure 4).

3 Causal Mechanisms

The existence of a flight of emergent marine terraces is consistent with stratigraphic and thermochronologic observations, revealing that Madagascar underwent regional uplift during Neogene times. In northern Madagascar, scattered remnants of horizontally bedded Eocene (~ 56–34 Ma) limestones occur at elevations of 300–500 m and contain abundant nummulites, which are marine protozoans (Figure 4a). The existence of these outcrops is consistent with an average uplift rate of ~ 10 m/Ma, since sea level at the beginning of Eocene times could have been as much as ~ 100 m higher than the present-day level (e.g. *Miller et al.*, 2011). Inverse modeling of fission track measurements demonstrates that rapid regional cooling, consistent with regional uplift and denudation, commenced within the last 20 Ma (*Stephenson*, 2019). *Dixey* (1960) and *Roberts et al.* (2012b) used geomorphic analysis of uplifted peneplains and inverse modeling of drainage networks to propose that Madagascar underwent wholesale regional uplift during Neogene times. These onshore observations are consistent with positive residual depth measurements from surrounding oceanic lithosphere, demonstrating that Madagascar sits on the uplifted fringes of the Southern Ocean superswell (Figures 1a and 5a; *Hoggard et al.*, 2016, 2017).

Geophysical and geochemical observations suggest that regional uplift is generated and maintained by mantle convective processes. The existence of a positive long wavelength (~ 10^3 km) free-air gravity anomaly is consistent with sub-plate support. This inference is corroborated by earthquake tomographic models which show that Madagascar is underlain by a significant negative shear wave velocity anomaly (Figure 5; *Fishwick*, 2010; *Schaeffer and Lebedev*, 2013; *Pratt et al.*, 2017). This anomaly is converted into temperature using the global calibration scheme described by *Yamauchi and Takei* (2016). Their scheme extends the analysis of *Priestley and McKenzie* (2013) by refining the conversion from shear wave velocity, V_s, to temperature, T, as the melting temperature is approached. The parameters used by *Yamauchi and Takei* (2016) for this V_s-T conversion are calibrated against the tomographic model of *Priestley and McKenzie* (2013). Here, we use the same parameter values to convert V_s into T for the tomographic model of *Schaeffer and Lebedev* (2013). We find that sub-plate asthenospheric mantle beneath northern Madagascar has a potential temperature of $T_p = 1380 \pm 30°$ C. This temperature is 50 ± 30 ° C hotter than ambient asthenospheric mantle (*Katz et al.*, 2003). It is crucial to emphasize that a similar temperature anomaly is obtained if the tomographic model of *Schaeffer and Lebedev* (2013) is independently calibrated with a revised plate model (F. Richards, pers. comm., 2019).

The existence and size of this sub-plate temperature anomaly are corroborated by two suites of independent observations. First, Neogene basaltic rocks are distributed throughout northern Madagascar (Figure 1e). Melt equilibration pressure and temperature estimates determined from the chemical composition of basaltic samples of Montagne d'Ambre using the thermobarometric approach of *Plank and Forsyth* (2016) are consistent with $T_p = 1390^{+85}_{-55}$ °C (Figure 5e and f). This estimate is probably an upper limit for sub-plate temperatures since equilibration temperatures obtained beneath mid oceanic ridges using this thermobarometric approach are higher than expected (*Lee et al.*, 2009; *Katz et al.*, 2003). Inverse modeling of observed distributions of rare earth elements for tholeiitic basalts from the Cap d'Ambre region yield $T_p = 1350 \pm 20$ °C beneath a lithospheric plate that is $\sim$ 60 km thick (*Klöcking*, 2017). Secondly, the isostatic consequences of this inferred asthenospheric temperature anomaly can be tested using offshore and onshore observations of long-term vertical motions. Regional uplift, U, is given by

$$U = \frac{2h\alpha\Delta T}{1 - \alpha T_\circ}, \tag{1}$$

where $2h = 150$ km is thickness of the hot sub-plate layer, ΔT is its average excess temperature, $T_\circ$ is the temperature of ambient mantle, and $\alpha = 3.28 \times 10^{-5}$ °C^{-1} is the coefficient of thermal expansion (*Rudge et al.*, 2008). In northern Madagascar, the predicted pattern of U closely agrees with that inferred from receiver function analyses and with residual depth anomalies measured offshore (Figure 5a). Significantly, the crust beneath northern Madagascar is only 18 ± 2 km thick, which means that its present-day elevation is isostatically anomalous and indicative of ongoing sub-plate support (Supplementary Material; *Andriampenomanana et al.*, 2017). The observed and predicted gradients of dynamic topography are between 1 and 8 in 10^4, reflecting the increasing amplitude of this asthenospheric temperature anomaly to the north (Figure 5d). It is unlikely that this northward gradient is generated by flexural loading associated with growth of the older (i.e. 12.1–0.83 Ma) volcanic edifice of Montagne d'Ambre (*Emerick and Duncan*, 1982; *Cucciniello et al.*, 2011). In northern Madagascar, there is also no evidence for large-scale active normal faulting (*Besairie*, 1964; *Rindraharisaona et al.*, 2013). Significantly, the gradient of emergent terraces requires the existence of a major north-south trending normal fault with a displacement since the last interglacial period of at least 200 m, which is not observed (Supplementary Material). It is important to emphasize that this thermal isostatic calculation intentionally sidesteps a much-debated question, namely what is the component of dynamic topography that is predicted to arise from viscous flow within the deeper mantle? We have avoided this issue for two significant reasons. First, there is much disagreement between different numerical models of viscous flow for the mantle with regard to both amplitude and wavelength of predicted dynamic topography. From a global perspective, there are also large discrepancies between observed and predicted power spectra of dynamic topography (*Hoggard et al.*, 2016). Secondly, our results suggest that epeirogenic uplift of northern Madagascar can be accounted for by the existence of a layer of anomalously hot asthenospheric mantle directly beneath a thin lithospheric plate, for which there is independent seismic and petrologic evidence. The dominance of this thermal isostatic signal means that our observations cannot easily be used to test competing numerical models of viscous flow of the deeper mantle.

Taken together, our self-consistent observations imply that emergent marine terraces, which rim northern Madagascar, reflect ongoing regional uplift caused by growth of a hot mantle upwelling. A significant corollary is that it is less likely these terraces are generated exclusively either by eustatic sea-level change or by glacio-isostatic adjustment. The undated upper terrace might represent MIS 11 but it may well be significantly older since it occurs at an elevation of 29.5–33.8 m, which exceeds any sea-level highstand during the last 1 Ma. Reliable outcrops of MIS 11 are reported at uncorrected heights of 14 ± 2 m around South Africa and of 21.3 ± 1.0 m on Bermuda, which is located within the forebulge of the Laurentide Ice Sheet (*Roberts et al.*, 2012a; *Hearty et al.*, 1999; *Olson and Hearty*, 2009). Modeling of glacio-isostatic adjustment yields corrected estimates of 6–13 m and 8.0–11.5 m, respectively (*Raymo and Mitrovica*, 2012; *Chen et al.*, 2014). Since the glacio-isostatic correction for South Africa is probably only a few meters, this observation alone suggests that the upper terrace of northern Madagascar could have been uplifted by at least 10–20 m (*Chen et al.*, 2014). We note in passing that there is a peneplain above the upper terrace at a height of ~ 50 m, which may represent Middle Pliocene sea level that is reported elsewhere at heights of 30 ± 18 m (*Dowsett and Cronin*, 1990; *Rovere et al.*, 2014).

Radiometric dates from the intermediate terrace correlate with MIS 5e and there is no evidence of a relationship between either uncorrected or corrected ages and terrace height. This absence suggests that there was no systematic regional change in relative sea level during the period of time over which the intermediate terrace formed. Field observations are consistent with a single sea-level highstand during MIS 5e, which resulted in the formation of the observed suite of sea-level markers. Published observations from Western Australia and from the Yucatán peninsula of Mexico imply that sea level remained relatively constant from the start of MIS 5e until a putative increase that post-dates 120 ka (*O'Leary et al.*, 2013; *Blanchon et al.*, 2009). Although we cannot rule out this possibility, we did not observe any evidence for a late increase in sea level toward the end of MIS 5e. Significantly, the morphology of this terrace remains remarkably consistent along our transect such that the gradient of the sandstone bench, the elevation of coral heads, and the height of the upper terrace are consistent with regional tilting and inconsistent with temporal variations of sea level during the interglacial period (Figures 4 and 5).

Although the intermediate terrace probably formed coevally at the same elevation during MIS 5e, glacio-isostatic adjustment can produce regional spatial and temporal variations, especially at the start of an interglacial period (e.g. *Mitrovica and Milne*, 2002; *Austermann et al.*, 2017). Continental levering, whereby hydrologic loading of an oceanic basin flexes the adjacent continental margin, can generate spatial gradients of sea level (*Nakada and Lambeck*, 1989). The narrow northern peninsula of Madagascar is probably flexurally down-loaded whilst further south, the continental interior is flexed upwards (e.g. *Nakada and Lambeck*, 1989). We apply the glacio-isostatic model described by *Austermann et al.* (2017) to calculate the effect of continental levering. We used their parameter values such that an elastic layer that is 71 km thick is assumed to overlie an upper mantle layer with a viscosity of 4×10^{20} Pa s and a lower mantle layer with a viscosity of 5×10^{22} Pa s. Tests show that varying these parameters within reasonable ranges does not affect our principal conclusions. A two-cycle ice history was constructed using the ICE-6G model for the last and penultimate interglacial periods and the glaciation phase was deemed to have followed the eustatic curve inferred by *Waelbroeck et al.* (2002). Along the northern rim of Madagascar, glacio-isostatic adjustment calculations show that the calculated gradient relative to present day has the opposite sense to that which is observed (Figure 6a). Thus, if the intermediate terrace formed at the start of the last interglacial period, the effect of the levering correction tends to exaggerate the observed gradient. Although the direction of this levering gradient reverses toward the end of the interglacial period, it is too modest to be the principal mechanism of formation of the observed gradient (Figure 6b). We conclude that the spatial gradient of this intermediate MIS 5e terrace cannot be accounted for either by eustatic sea-level change or by glacio-isostatic adjustment. Similar arguments apply to the elevation of the more sporadically observed lower terrace, which coincides with the Holocene transgression, and whose height within equatorial latitudes has been attributed to glacio-isostatic siphoning.

4 Implications and Conclusions

Dramatic gradients in heights of emergent marine terraces that rim northern Madagascar are documented. For example, elevation of a spectacularly exposed MIS 5e coral-rich terrace decreases from 9.3 m to 2.8 m over a distance of 80 km. It is evident that, in this case, calculations based upon glacio-isostatic adjustment models cannot match this gradient. Furthermore, the heights and gradients of overlying and underlying terraces have similar patterns. Instead, we suggest that these gradients are generated and maintained by sub-plate convective upwelling of hot mantle material. Diverse geophysical and geochemical observations imply that Madagascar is undergoing rapid regional uplift that started in Neogene times. The scale of regional uplift can be quantified using earthquake tomographic models which demonstrate that northern Madagascar is underlain by a slow shear wave velocity anomaly that is $\sim 150 \pm 75$ km thick. Global calibration of shear wave velocity anomalies suggests that this anomaly is a manifestation of elevated asthenospheric temperatures that are consistent with independent estimates based upon thermobarometric and geochemical modeling of basaltic igneous rocks.

This Malagasy study has two far-reaching implications. First, our results highlight the short timescales and length scales over which dynamic topography evolves. Eastward migration of Madagascar relative to Africa is slow (i.e. < 5 mm/yr; *Saria et al.*, 2014). Hence, the evolution of dynamic topography probably arises from changes in the sub-lithospheric pattern of convection. This inference is consistent with previous observational and modeling studies that also suggest that dynamic topography can evolve rapidly and on short length scales (*Hartley et al.*, 2011; *Parnell-Turner et al.*, 2013; *Hoggard et al.*, 2016; *Walker et al.*, 2016). Secondly, it is evident that heights of MIS 5e sea-level markers vary globally along continental margins (Figure 1a, b). In Western Australia, these markers occur at an elevation of 2.5 m, in South Africa, they occur at 6–8 m, whilst in Angola they are observed at heights of up to 25 m (*Carr et al.*, 2009; *Guiraud et al.*, 2010; *O'Leary et al.*, 2013; *Walker et al.*, 2016). A combination of offshore stratigraphic and onshore geologic observations show that the Angolan margin has been dynamically uplifted whereas the Western Australian margin has been convectively drawn-down (*Al-Hajri et al.*, 2009; *Czarnota et al.*, 2013). *Austermann et al.* (2017) argue that some fraction of the elevation of MIS 5e terrace height is expected to be generated by dynamic topography. Our results cohere with their suggestion and provide exciting evidence that these changes can be mapped along coastal transects. Hence, there is the prospect that dynamic topographic components of sea-level marker heights can be disentangled from eustatic sea-level variations by careful observations. A detailed study of sea-level markers will help to elucidate both the height of the MIS 5e highstand, as well as Quaternary vertical movements of the Earth's surface.

Acknowledgements

SNS is funded by the University of Cambridge. We are grateful to B. Ralison, N. Raberehareha, M. Rajaobelison, L. Rahantarisoa and R. Razafimbelo for their assistance in the field and to J. Austermann for carrying out the glacio-isostatic adjustment calculations. We also thank S. Cable, A. Copley, I. Frame, M. Hoggard, D. Lyness, C. O'Malley, J. Paul, F. Richards, G. Roberts and N. Santodomingo for their help. Department of Earth Sciences contribution number esc.XXXX.

References

Al-Hajri, Y., N. White, and S. Fishwick (2009), Scales of transient convective support beneath Africa, *Geology*, *37*(10), 883–886, doi:10.1130/G25703A.1.

Andriampenomanana, F., A. A. Nyblade, M. E. Wysession, R. J. Durrheim, F. Tilmann, J. Juli, M. J. Pratt, G. Aleqabi, P. J. Shore, and T. Rakotondraibe (2017), The structure of the crust and uppermostmantle beneath Madagascar, *Geophysical Journal International*, *210*, 1525–1544, doi:10.1093/gji/ggx243.

Austermann, J., J. X. Mitrovica, P. Huybers, and A. Rovere (2017), Detection of a dynamic topography signal in last interglacial sea-level records, *Science Advances*, *3*(July), 1–9.

Battistini, R. (1959), Note Preliminaire sur l'existence de deux periodes pluviales de Demantelement de la Grande Dunes petrifee du sud de l'Androy, *La Naturaliste Malgache*, *X1*(1-2).

Battistini, R. (1965), Le Quaternaire littoral de l'extreme nord de Madagascar, *Bulletin d'Association francaise pour l'etude du quaternaire*, *2*(2), 134–144.

Battistini, R. (1977), Ages absolus Th^{230}/U^{234} de depots marins Pleistocenes a Madagascar et dans les Iles Voisines, *Madagascar Revues de Geographie*, *31*, 73–86.

Becker, J. J., D. T. Sandwell, W. H. Smith, J. Braud, B. Binder, J. Depner, D. Fabre, J. Factor, S. Ingalls, S. H. Kim, R. Ladner, K. Marks, S. Nelson, A. Pharaoh, R. Trimmer, J. von Rosenberg, G. Wallace, and P. Weatherall (2009), Global bathymetry and elevation data at 30 arc seconds resolution: SRTM30_PLUS, *Marine Geodesy*, *32*(4), 355–371, doi:10.1080/01490410903297766.

Besairie, H. (1964), Carte Géologique de Madagascar, au 1:1,000,000, trois feuilles en couleur.

Blanchon, P., A. Eisenhauer, J. Fietzke, and V. Liebetrau (2009), Rapid sea-level rise and reef back-stepping at the close of the last interglacial highstand, *Nature*, *458*(7240), 881–884, doi:10.1038/nature07933.

Carr, A. S., M. D. Bateman, D. L. Roberts, C. V. Murray-wallace, Z. Jacobs, and P. J. Holmes (2009), The last interglacial sea-level high stand on the southern Cape coastline of South Africa, *Quaternary Research*, *73*(2), 351–363, doi:10.1016/j.yqres.2009.08.006.

Chen, A. T., L. F. Robinson, A. Burke, J. Southon, P. Spooner, P. J. Morris, and H. C. Ng (2015), Synchronous sub-millennial scale abrupt events in the ocean and atmosphere during the last deglaciation, *Science*, *1*(May), 1537–1542, doi:10.1126/science.aac6159.

Chen, F., S. Friedman, C. G. Gertler, J. Looney, N. O'Connell, K. Sierks, and J. X. Mitrovica (2014), Refining estimates of polar ice volumes during the MIS11 interglacial using sea level records from South Africa, *Journal of Climate*, *27*(23), 8740–8746, doi:10.1175/JCLI-D-14-00282.1.

Cucciniello, C., L. Melluso, V. Morra, M. Storey, I. Rocco, L. Franciosi, C. Grifa, C. Petrone, and M. Vincent (2011), New ^{40}Ar-^{39}Ar ages and petrogenesis of the Massif d'Ambre volcano, northern Madagascar, in *Volcanism and Evolution of the African Lithosphere*, edited by L. Beccaluva, G. Bianchini, and M. Wilson, pp. 257–281, The Geological Society of America, doi:10.1130/2011.2478(14).

Czarnota, K., M. J. Hoggard, N. White, and J. Winterbourne (2013), Spatial and temporal patterns of Cenozoic dynamic topography around Australia, *14*(3), 634–658, doi: 10.1029/2012GC004392.

Dixey, F. (1960), The geology and geomorphology of Madagascar and a comparison with eastern Africa, *Quarterly Journal of the Geological Society*, *116*, 255–268.

Dowsett, H. J., and T. M. Cronin (1990), High eustatic sea level during the middle Pliocene:Evidence from the southeastern U.S. Atlantic Coastal Plain, *Geology*, *18*(5), 435, doi:10.1130/0091-7613(1990)018<0435:HESLDT>2.3.CO;2.

Dutton, A., and K. Lambeck (2012), Ice Volume and Sea Level During the Last Interglacial, *Science*, *216*(July), 216–220, doi:10.1126/science.1205749.

Dutton, A., A. E. Carlson, A. J. Long, G. A. Milne, P. U. Clark, R. DeConto, B. P. Dorton, S. Rahmstorf, and M. E. Raymo (2015), Sea-level rise due to polar ice-sheet mass loss during past warm periods, *Science*, *349*(6244), 153–162, doi:10.1126/science.aaa4019.

Egbert, G. D., and S. Y. Erofeeva (2002), Efficient inverse modeling of barotropic ocean tides, *Journal of Atmospheric and Oceanic Technology*, *19*(2), 183–204, doi:10.1175/1520-0426(2002)019<0183:EIMOBO>2.0.CO;2.

Emerick, C. M., and R. A. Duncan (1982), Age progressive volcanism in the Comores Archipelago, western Indian Ocean and implications for Somali plate tectonics, *Earth and Planetary Science Letters*, *60*(3), 415–428, doi:10.1016/0012-821X(82)90077-2.

Farrell, E. W., and A. J. Clark (1976), On Postglacial Sea Level, *Geophysical Journal of the Royal Astronomical Society*, *46*(3), 647–667, doi:10.1111/j.1365-246X.1976.tb01252.x.

Fishwick, S. (2010), Surface wave tomography: imaging of the lithosphere – asthenosphere boundary beneath central and southern Africa, *Lithos*, *120*(1-2), 63–73, doi: 10.1016/j.lithos.2010.05.011.

Guiraud, M., A. Buta-Neto, and D. Quesne (2010), Segmentation and differential post-rift uplift at the Angola margin as recorded by the transform-rifted Benguela and oblique-to-orthogonal-rifted Kwanza basins, *Marine and Petroleum Geology*, *27*(5), 1040–1068, doi: 10.1016/j.marpetgeo.2010.01.017.

Hartley, R. A., G. G. Roberts, N. White, and C. Richardson (2011), Transient convective uplift of an ancient buried landscape, *Nature Geoscience*, *4*(8), 562–565, doi:10.1038/ngeo1191.

Hearty, P. J., P. Kindler, H. Cheng, and R. L. Edwards (1999), A +20 m middle Pleistocene sea-level highstand (Bermuda and the Bahamas) due to partial collapse of Antartic ice, *Geology*, *27*(4), 375–378, doi:10.1130/0091-7613(1999)027<0375.

Hibbert, F. D., E. J. Rohling, A. Dutton, F. H. Williams, P. M. Chutcharavan, C. Zhao, and M. E. Tamisiea (2016), Coral indicators of past sea-level change : A global repository of U-series dated benchmarks, *Quaternary Science Reviews*, *145*, 1–56, doi:10.1016/j.quascirev.2016.04.019.

Hoggard, M. J., N. White, and D. Al-Attar (2016), Global dynamic topography observations reveal limited influence of large-scale mantle flow, *Nature Geoscience*, (May), doi:10.1038/ngeo2709.

Hoggard, M. J., J. Winterbourne, K. Czarnota, and N. White (2017), Oceanic residual depth measurements, the plate cooling model, and global dynamic topography, *Journal of Geophysical Research: Solid Earth*, *122*(May), 2328–2373, doi:10.1002/2016JB013457.

Katz, R. F., M. Spiegelman, and C. H. Langmuir (2003), A new parameterization of hydrous mantle melting, *Geochemistry, Geophysics, Geosystems*, *4*(9), 1–19, doi:10.1029/2002GC000433.

Klöcking, M. (2017), Continental Magmatism and Dynamic Topography, Ph.D. thesis, University of Cambridge.

Kopp, R. E., F. J. Simons, J. X. Mitrovica, A. C. Maloof, and M. Oppenheimer (2009), Probabilistic assessment of sea level during the last interglacial stage, *Nature*, *462*(7275), 863–867, doi: 10.1038/nature08686.

Lee, C. T. A., P. Luffi, T. Plank, H. Dalton, and W. P. Leeman (2009), Constraints on the depths and temperatures of basaltic magma generation on Earth and other terrestrial planets using new thermobarometers for mafic magmas, *Earth and Planetary Science Letters*, *279*(1-2), 20–33, doi:10.1016/j.epsl.2008.12.020.

McNab, F., P. W. Ball, M. J. Hoggard, and N. J. White (2018), Neogene Uplift and Magmatism of Anatolia: Insights From Drainage Analysis and Basaltic Geochemistry, *Geochemistry, Geophysics, Geosystems*, *19*(1), 175–213, doi:10.1002/2017GC007251.

Miller, K., G. Mountain, J. Wright, and J. Browning (2011), Sea level and ice volume variations from Continental Margins and Deep-Sea Isotopic Records, *Oceanography*, *24*(2), 40–53, doi: 10.5670/oceanog.2011.26.

Milne, G. A., J. X. Mitrovica, and D. P. Schrag (2002), Estimating past continental ice volume from sea-level data, *Quaternary Science Reviews*, *21*(1-3), 361–376, doi:10.1016/S0277-3791(01)00108-1.

Mitrovica, J. X., and G. A. Milne (2002), On the origin of late Holocene sea-level highstands within equatorial ocean basins, *Quaternary Science Reviews*, *21*, 2179–2190.

Mitrovica, J. X., and W. R. Peltier (1991), On Postglacial Geoid Subsidence Over the Equatorial Ocean, *Journal of Geophyical Research*, *96*, 2053–2071.

Nakada, M., and K. Lambeck (1989), Late Pleistocene and Holocene sea-level change in the Australian region and mantle rheology, *Geophysical Journal International*, *96*(1989), 497–517.

O'Leary, M. J., P. J. Hearty, W. G. Thompson, M. E. Raymo, J. X. Mitrovica, and J. M. Webster (2013), Ice sheet collapse following a prolonged period of stable sea level during the last interglacial, *Nature Geoscience*, *6*(9), 796–800, doi:10.1038/ngeo1890.

Olson, S. L., and P. J. Hearty (2009), A sustained +21 m sea-level highstand during MIS 11 (400 ka): direct fossil and sedimentary evidence from Bermuda, *Quaternary Science Reviews*, *28*(3-4), 271–285, doi:10.1016/j.quascirev.2008.11.001.

Parnell-Turner, R. E., N. J. White, J. MacLennan, T. J. Henstock, B. J. Murton, and S. M. Jones (2013), Crustal manifestations of a hot transient pulse at 60°N beneath the Mid-Atlantic Ridge, *Earth and Planetary Science Letters*, *363*, 109–120, doi:10.1016/j.epsl.2012.12.030.

Pedoja, K., L. Husson, V. Regard, P. R. Cobbold, E. Ostanciaux, M. E. Johnson, S. Kershaw, M. Saillard, J. Martinod, L. Furgerot, P. Weill, and B. Delcaillau (2011), Relative sea-level fall since the last interglacial stage: Are coasts uplifting worldwide?, *Earth-Science Reviews*, *108*(1-2), 1–15, doi:10.1016/j.earscirev.2011.05.002.

Plank, T., and D. W. Forsyth (2016), Thermal structure and melting conditions in the mantle beneath the Basin and Range province from seismology and petrology, *Geochemistry Geophysics Geosystems*, *17*, 2825–2834, doi:10.1002/2016GC006406.

Pratt, M. J., M. E. Wysession, G. Aleqabi, D. A. Wiens, A. A. Nyblade, P. Shore, G. Rambolamanana, F. Andriampenomanana, T. Rakotondraibe, R. D. Tucker, G. Barruol, and E. Rindraharisaona (2017), Shear velocity structure of the crust and upper mantle of Madagascar derived from surface wave tomography, *Earth and Planetary Science Letters*, *458*, 405–417, doi:10.1016/j.epsl.2016.10.041.

Priestley, K., and D. McKenzie (2013), The relationship between shear wave velocity, temperature, attenuation and viscosity in the shallow part of the mantle, *Earth and Planetary Science Letters*, *381*, 78–91, doi:10.1016/j.epsl.2013.08.022.

Raymo, M. E., and J. X. Mitrovica (2012), Collapse of polar ice sheets during the stage 11 interglacial, *Nature*, *483*(7390), 453–456, doi:10.1038/nature10891.

Rindraharisaona, E. J., M. Guidarelli, A. Aoudia, and G. Rambolamanana (2013), Earth structure and instrumental seismicity of Madagascar: Implications on the seismotectonics, *Tectonophysics*, *594*, 165–181, doi:10.1016/j.tecto.2013.03.033.

Ritsema, J., A. Deuss, H. J. Van Heijst, and J. H. Woodhouse (2011), S40RTS: A degree-40 shear-velocity model for the mantle from new Rayleigh wave dispersion, teleseismic traveltime and normal-mode splitting function measurements, *Geophysical Journal International*, *184*(3), 1223–1236, doi:10.1111/j.1365-246X.2010.04884.x.

Roberts, D. L., P. Karkanas, Z. Jacobs, C. W. Marean, and R. G. Roberts (2012a), Melting ice sheets 400,000 yr ago raised sea level by 13 m: Past analogue for future trends, *Earth and Planetary Science Letters*, *357-358*, 226–237, doi:10.1016/j.epsl.2012.09.006.

Roberts, G. G., J. D. Paul, N. White, and J. Winterbourne (2012b), Temporal and spatial evolution of dynamic support from river profiles: A framework for Madagascar, *Geochemistry, Geophysics, Geosystems*, *13*(4), 1–23, doi:10.1029/2012GC004040.

Rohling, E. J., K. Grant, C. H. Hemleben, M. Siddall, B. A. A. Hoogakker, M. Bolshaw, and M. Kucera (2008), High rates of sea-level rise during the last interglacial period, *Nature Geoscience*, *1*, 38–42, doi:10.1038/ngeo.2007.28.

Rovere, A., M. E. Raymo, J. X. Mitrovica, P. J. Hearty, M. J. O'Leary, and J. D. Inglis (2014), The Mid-Pliocene sea-level conundrum: Glacial isostasy, eustasy and dynamic topography, *Earth and Planetary Science Letters*, *387*, 27–33, doi:10.1016/j.epsl.2013.10.030.

Rovere, A., M. E. Raymo, M. Vacchi, T. Lorscheid, P. Stocchi, L. Gómez-pujol, D. L. Harris, E. Casella, M. J. O. Leary, and P. J. Hearty (2016), The analysis of last interglacial (MIS 5e) relative sea-level indicators: reconstructing sea-level in a warmer world, *Earth Science Reviews*, *159*, 404–427, doi:10.1016/j.earscirev.2016.06.006.

Rudge, J. F., M. E. Shaw Champion, N. White, D. McKenzie, and B. Lovell (2008), A plume model of transient diachronous uplift at the Earth's surface, *Earth and Planetary Science Letters*, *267*(1-2), 146–160, doi:10.1016/j.epsl.2007.11.040.

Saria, E., E. Calais, D. S. Stamps, D. Delvaux, and C. J. H. Hardnaty (2014), Present-day kinematics of the East African Rift, *Journal of Geophysical Research: Solid Earth*, *119*, 3584–3600, doi: 10.1002/2014JB011237.

Schaeffer, A. J., and S. Lebedev (2013), Global shear speed structure of the upper mantle and transition zone, *Geophysical Journal International*, *194*(1), 417–449, doi:10.1093/gji/ggt095.

Siddall, M., E. Rohling, A. Almogi-Labin, C. Hemleben, D. Meischner, I. Schmelzer, and D. A. Smeed (2003), Sea-level fluctuations during the last glacial cycle, *Nature*, *423*(June), 853–858, doi:10.1038/nature01687.1.

Stephenson, S. (2019), Dynamic Topography of Madagascar and its Surroundings, Ph.D. thesis, Univeristy of Cambridge.

Tapley, B., J. Ries, S. Bettadpur, D. Chambers, M. Cheng, F. Condi, B. Gunter, Z. Kang, P. Nagel, R. Pastor, T. Pekker, S. Poole, and F. Wang (2005), GGM02 - An improved Earth gravity field model from GRACE, *Journal of Geodesy*, *79*(8), 467–478, doi:10.1007/s00190-005-0480-z.

Thompson, W. G., M. W. Spiegelman, S. L. Goldstein, and R. C. Speed (2003), An open-system model for U-series age determinations of fossil corals, *Earth and Planetary Science Letters*, *210*, 365–381, doi:10.1016/S0012-821X(03)00121-3.

Waelbroeck, C., L. Labeyrie, E. Michel, J. Duplessy, J. McManus, K. Lambeck, B. Balbon, and M. Labracherie (2002), Sea-level and deep water temperature changes derived from benthic foraminifera isotopic records, *Quaternary Science Reviews*, *21*, 295–305.

Walcott, R. I. (1972), Past sea levels, eustasy and deformation of the earth, *Quaternary Research*, *2*(1), 1–14, doi:10.1016/0033-5894(72)90001-4.

Walker, R. T., M. Telfer, R. L. Kahle, M. W. Dee, B. Kahle, J. Schwenninger, R. A. Sloan, and A. B. Watts (2016), Rapid mantle-driven uplift along the Angolan margin in the late Quaternary, *Nature Geoscience*, *9*, 909–916, doi:10.1038/NGEO2835.

Yamauchi, H., and Y. Takei (2016), Polycrystal anelasticity at near-solidus temperatures, *Journal of Geophysical Research: Solid Earth*, *121*(11), 7790–7820, doi:10.1002/2016JB013316.

Sample	Latitude	Longitude	Conventional age, ka	$\pm 2\sigma$	$\delta^{234}U_i$	$\pm 2\sigma$	Corrected age, ka	$\pm 2\sigma$
1	-11.95455	49.27193	165.5	2.1	244.5	2.0	125.5	1.8
2	-11.96620	49.27790	126.2	1.3	157.8	1.5	121.8	1.5
3	-11.96482	49.27710	3.8	0.3	147.0	1.1	-	-
4	-12.24060	49.37508	151.9	6.7	177.1	4.6	139.0	5.3
5	-12.24058	49.37525	141.9	2.5	158.9	2.7	136.9	2.3
6	-12.41098	49.52975	152.0	1.6	201.4	1.9	129.4	1.8
7	-12.60669	49.55818	149.3	1.7	164.6	1.7	141.8	1.9
8	-12.60669	49.55818	132.4	1.8	160.8	2.1	126.6	2.0
9	-12.60578	49.55886	134.5	1.9	165.2	2.1	126.9	1.8
10	-12.60567	49.55908	140.9	2.0	177.2	2.3	128.3	1.9
11*	-12.10507	49.08543	-0.6	0.3	146.6	1.1	-	-
12	-12.10658	49.08525	3.5	0.1	147.7	1.2	-	-
13	-12.10868	49.08475	1.6	0.9	147.0	1.4	-	-

Table 1: U-Th dating of corals sampled in northern Madagascar. Corrected age = date corrected for diagenetic processes (*Thompson et al.*, 2003). * indicates modern coral.

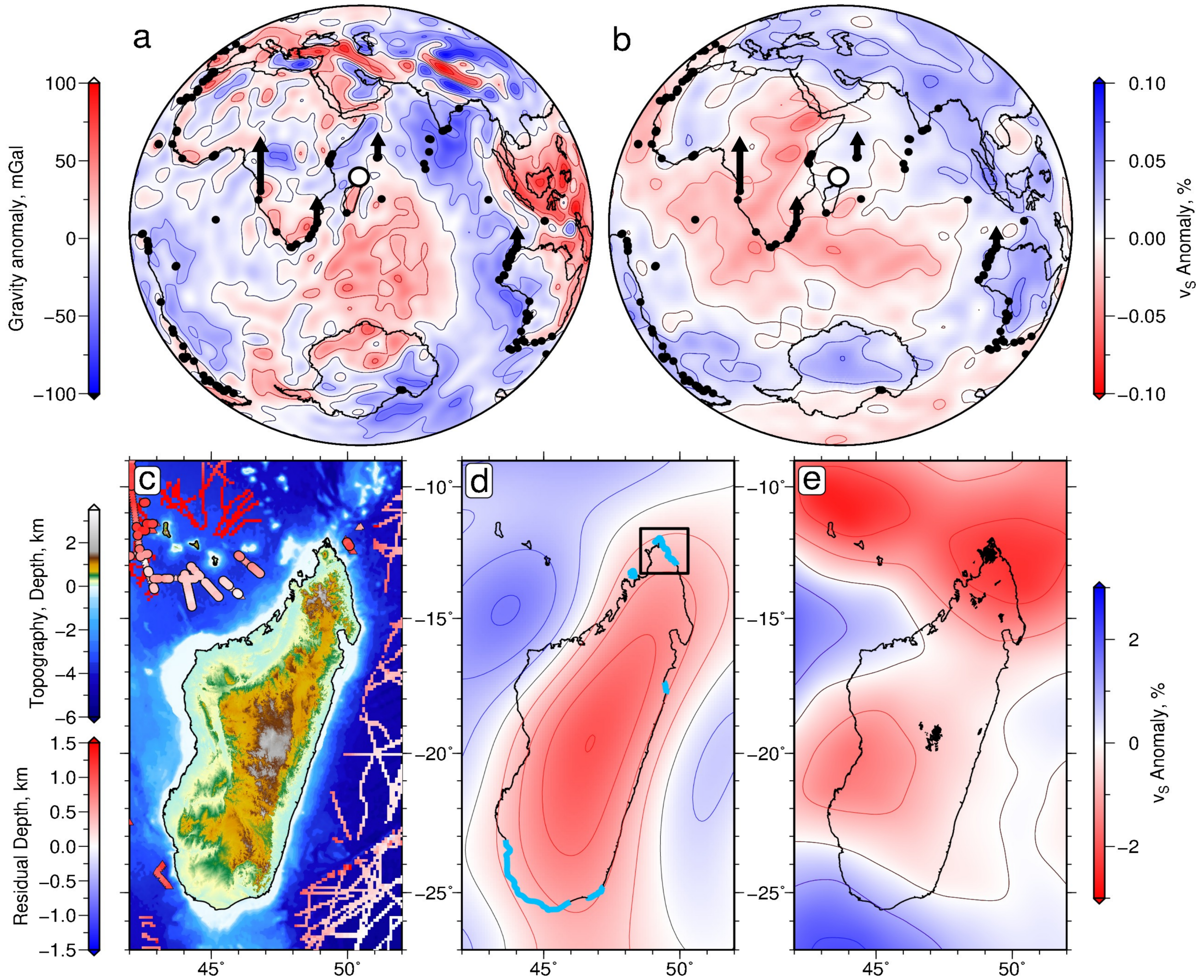

Figure 1: (a) Long wavelength (i.e. > 800 km) free-air gravity field from GGMO3C model (*Tapley et al.*, 2005). Black circles = MIS 5e sea-level markers from continental margins and oceanic islands (*Austermann et al.*, 2017); large open circle = sites from northern Madagascar described in this study; arrows of variable length = loci/height of emergent MIS 5e marine terraces from Angola (∼ 25 m; *Guiraud et al.*, 2010), South Africa (∼ 7 m; *Carr et al.*, 2009), Seychelles (∼ 7.6 ± 1.7 m; *Dutton et al.*, 2015) and Western Australia (∼ 2.5 m; *O'Leary et al.*, 2013). (b) Average shear-wave velocity anomaly for whole mantle calculated from S40RTS tomographic model (*Ritsema et al.*, 2011). Black circles and large open circle as before. (c) Topographic and bathymetric map of Madagascar calculated using 3 arc second SRTM and ETOPO1 digital databases (*Becker et al.*, 2009). Colored circles = water-loaded residual depth estimates corrected for both sedimentary and crustal loading (*Hoggard et al.*, 2017); colored upward-/downward-pointing triangles = upper/lower bounds for water-loaded residual depth where only sedimentary loading is corrected; colored linear tracks = shiptrack bathymetric measurements corrected for sediment thickness from global grid (*Hoggard et al.*, 2017). (d) Map of estimated dynamic topography calculated from long wavelength free-air gravity anomalies using admittance of Z = 45 mGal km^{-1} with scale bar shown on left-hand side of panel (c). Turquoise lines = emergent Pleistocene reef deposits (e.g. *Battistini*, 1959, 1965, 1977) and this study; black box = region of this study. (e) Map of shear wave velocity anomaly at depth of 125 km (*Schaeffer and Lebedev*, 2013). Black polygons = Neogene volcanic rocks.

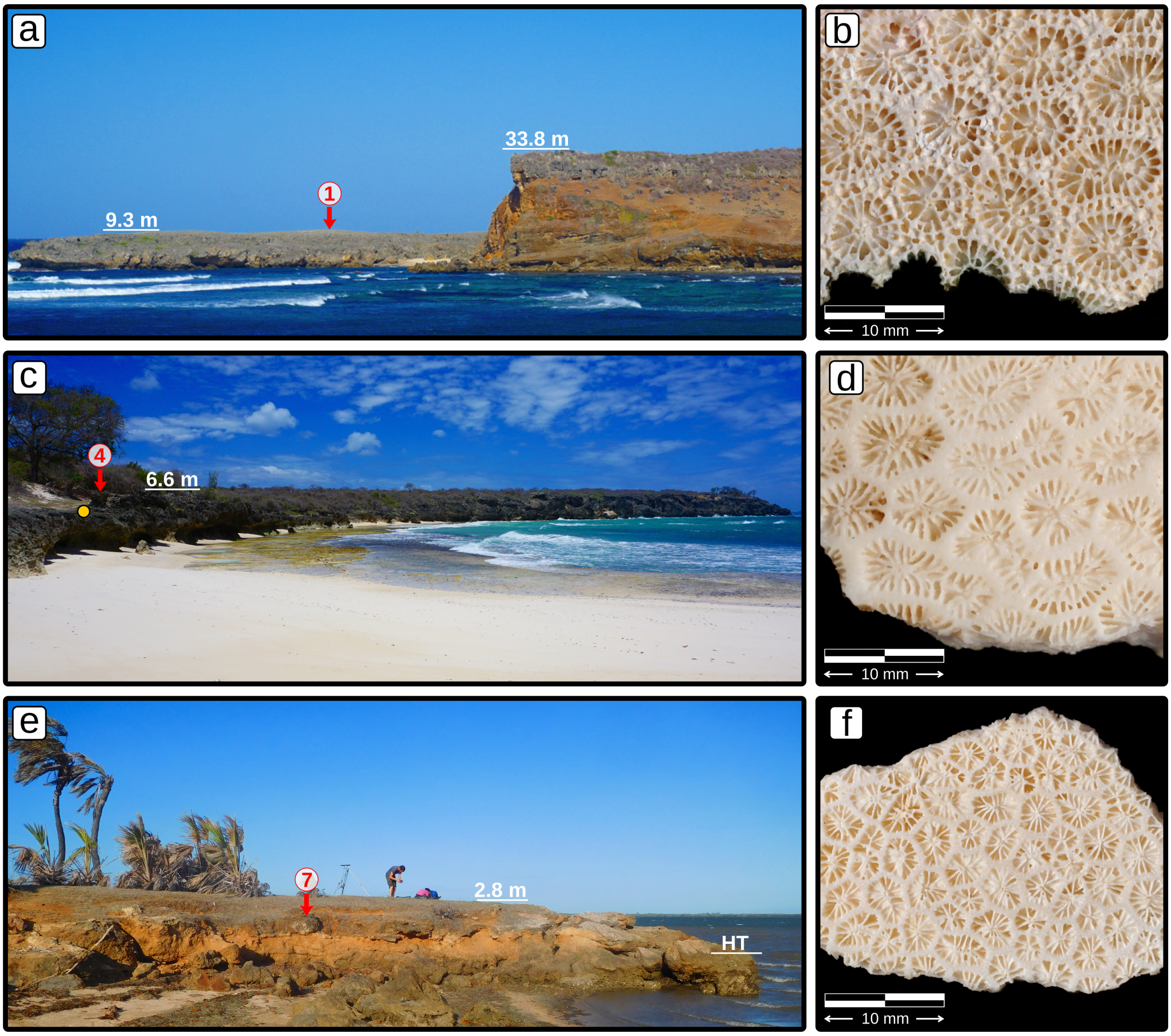

Figure 2: Emergent coral reef deposits of northern Madagascar. (a) View looking east at Cap d'Ambre on northern tip of Madagascar (Figure 4). Gray spit with flat top at 9.3 m elevation above mean low water springs datum = intermediate reef deposit (named Reef 2 by *Battistini*, 1965); lower half of prominent cliff with brown seaward-dipping foreset beds = volcaniclastic turbiditic deposits; upper half of cliff capped with gray layer with flat top at 33.8 m elevation above mean low water springs datum = upper reef deposit (i.e. Reef 1); numbered red circle with red arrow = location of coral sample (Table 1). (b) Coral specimen *Dipsastraea pallida* collected from top of intermediate terrace (see panel (a) for location). (c) View looking north at Orangea, located 35 km southeast of Cap d'Ambre (Figure 4). Gray bench with flat top at 4.6 m elevation above mean low water springs datum = intermediate reef deposit with coral heads protruding up to 6.6 m above mean low water springs datum; yellow circle = top of sandstone bench; numbered red circle with red arrow = location of coral sample (Table 1). (d) Coral specimen *Porites lobata* collected from top of intermediate terrace (see panel (c) for location). (e) View looking north at Irodo located 80 km south southeast of Cap d'Ambre (Figure 4). Grassy bench with flat top at 1 m above high-tide mark (HT), 2.8 m above mean low water springs datum = intermediate reef deposit; numbered red circle with red arrow = location of coral sample (Table 1). (f) Coral specimen *Goniastrea retiformis* collected from top of intermediate terrace (see panel (e) for location).

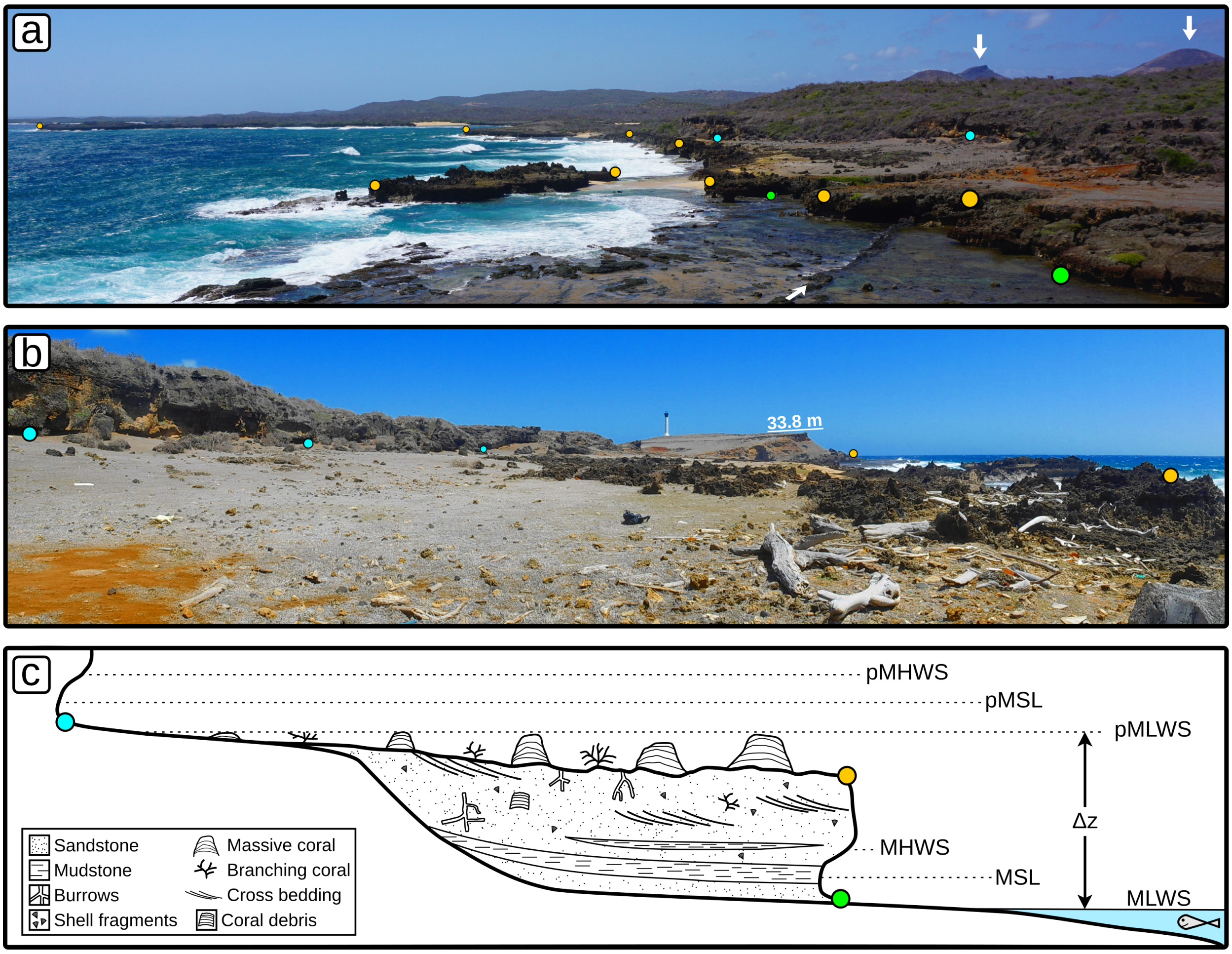

Figure 3: Morphology of intermediate terrace at Cap d'Ambre. (a) Photograph taken at lighthouse at Cap d'Ambre, viewing south. Green dots = location of modern tidal notch; yellow dots = location of outer margin of sandstone bench; blue dots = location of paleo tidal notch; white arrows = Neogene volcanoes and mafic dyke. (b) Panoramic photograph of intermediate terrace showing wavecut platform, coral heads and paleo tidal notch viewing north towards lighthouse at Cap d'Ambre. (c) Cartoon cross section through intermediate terrace morphology. Coloured dots = as panel (a); key to geological symbols shown in bottom left-hand corner; MHWS = mean high water springs; MSL = mean sea level; MLWS = mean low water springs; p prefix = paleo sea-level datums; Δz = difference in height between modern and paleo sea-level markers.

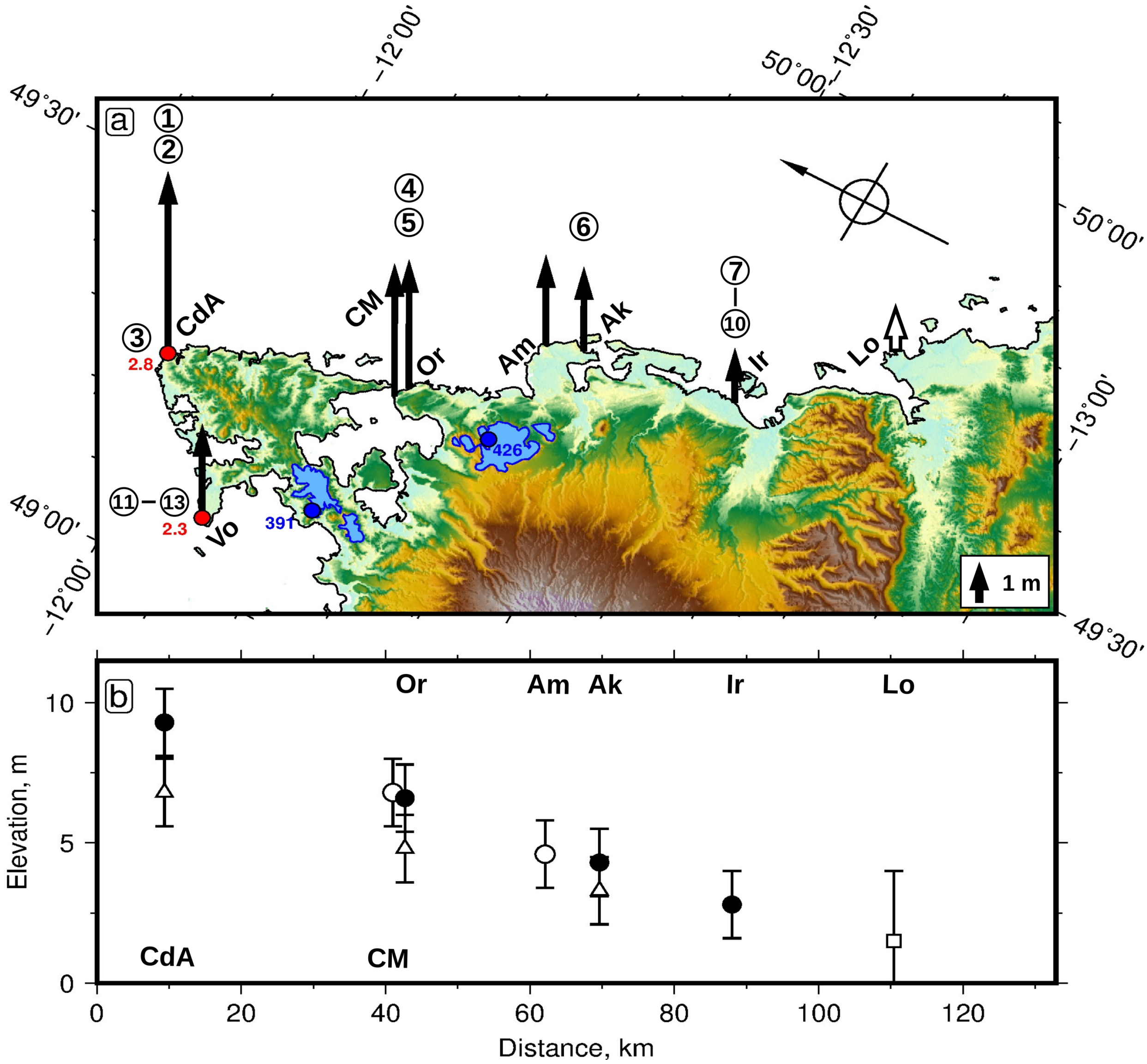

Figure 4: (a) Map of northern Madagascar showing location of coral reef deposits and raised beaches where radiometric dating was carried out. Numbered and scaled solid arrows = locations showing elevation of MIS 5e sea-level markers observed in this study (see Table 1); open arrow = location showing elevation of MIS 5e marker observed by *Battistini* (1965); numbered red circles = locations of Holocene sea-level markers showing meters elevation above mean low water springs datum; blue polygons = significant outcrops of Eocene nummulitic limestone; numbered blue circle = spot measurements of highest elevations of limestone; Vo = Vohilava, CdA = Cap d'Ambre, CM = Cap Miné, Or = Orangea, Am = Ambodivahibe, Ak = Ankirikiriky Bay, Ir = Irodo Bay, Lo = Loky Bay. (b) Elevation of MIS 5e sea-level markers plotted as function of distance along coastal transect. Solid circles = elevations of dated MIS 5e sea-level markers; open circles = elevations of stratigraphically correlated MIS 5e markers; open square = elevation of undated terrace height from *Battistini* (1965); open triangles = elevations of bioturbated sandstone benches that indicate base of coral-rich deposit. In each case, error bars reflect cumulative uncertainties that arise from locating high-tide mark, elevation surveying, and tidal corrections (see main text).

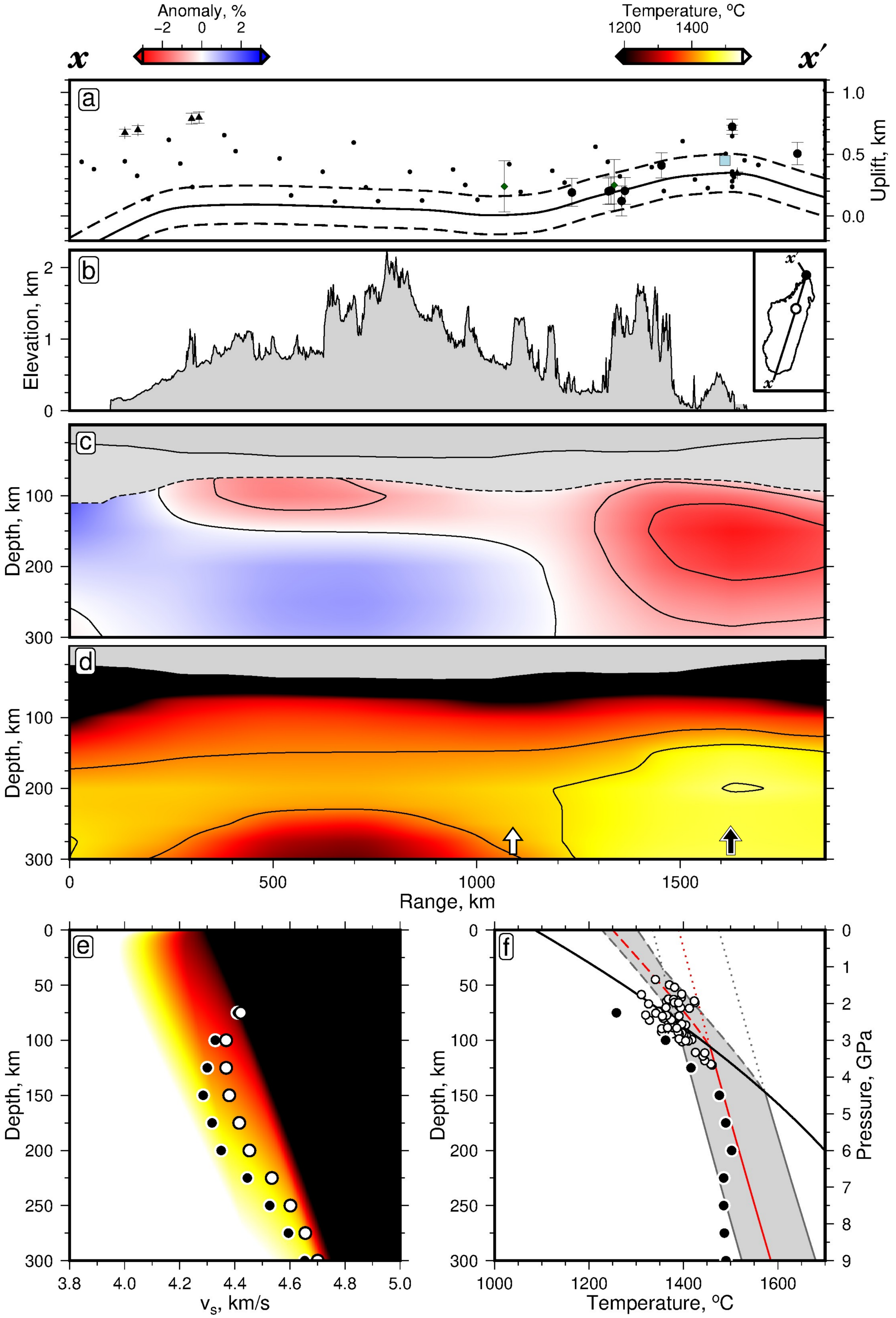

Anomaly, %
−2 0 2
Temperature, ºC
1200 1400
x
x′
a
Uplift, km
1.0
0.5
0.0
b
Elevation, km
2
1
0
c
Depth, km
100
200
300
d
Range, km
0 500 1000 1500
e
vs, km/s
3.8 4.0 4.2 4.4 4.6 4.8 5.0
f
Temperature, ºC
1000 1200 1400 1600
Pressure, GPa
0 1 2 3 4 5 6 7 8 9

Figure 5 ***(previous page)*****:** SW-NE transect, indicated by x–x', showing relationship between regional uplift, topography, tomography and inferred temperature (location of transect shown as inset of panel b). (a) Observed and calculated regional uplift. Solid/dashed lines = air-loaded uplift calculated using inferred sub-plate temperature anomaly shown in panel d for ambient asthenospheric potential temperature of 1330 ± 30 °C. Large black circles with error bars = regional air-loaded residual depth measurements, where both sedimentary and crustal corrections are applied, taken from *Hoggard et al.* (2017) and projected onto transect as necessary; upward/ downward pointing triangles = lower/upper estimates of residual depth for which only sedimentary correction is applied (sign of crustal correction inferred from regional constraints); small black circles = air-loaded residual depth measurements determined from ship-track inventory binned every 1°; blue square = elevation of Eocene nummulitic limestone that crops out in northernmost Madagascar; green diamonds with vertical bars = regional uplift $\pm 1\sigma$ determined by inverse modeling of apatite fission track measurements (*Stephenson*, 2019). (b) Topography along transect. (c) Vertical slice through earthquake tomographic model of *Schaeffer and Lebedev* (2013) where red/blue colors indicate negative/positive shear wave velocity anomalies relative to their version of AK135 global reference model adjusted for variable crustal structure. Gray polygon = lithospheric plate where calculated temperature < 1300°C; dashed line = locus of 1300°C isothermal surface; solid line = position of Moho discontinuity (*Andriampenomanana et al.*, 2017); white/black arrows = loci of two calculated geothermal profiles shown in panels e and f. (d) Vertical slice showing temperature structure determined by converting absolute shear wave velocities into temperatures (*Yamauchi and Takei*, 2016). White/black arrows = loci of two calculated geothermal profiles shown in panels e and f. (e) Contour map = temperature plotted as function of shear wave velocities, $V_s(z)$, and depth based on *Yamauchi and Takei* (2016)'s conversion scheme. White/black circles = $V_s(z)$ beneath northern Madagascar (see arrows in panel d). (f) Pressure-temperature calculations. Black circles = geothermal profile beneath northernmost Madagascar determined using V_s conversion scheme shown in panel d. Small white circles = pressure and temperature estimates determined from primary melt compositions of samples analyzed by *Cucciniello et al.* (2011) and by *Klöcking* (2017). Pressures and temperatures were calculated using mafic thermobarometric method of *Plank and Forsyth* (2016) assuming $Fe^{3+}/\Sigma Fe = 0.3$ and $Ce/H_2O = 200$ (*McNab et al.*, 2018). Uncertainties in pressure and temperature estimates have been determined for range of H_2O and Fe oxidation contents (*McNab et al.*, 2018, see body text). Pressure-temperature estimates are compared to anhydrous melt paths (gray polygon) calculated using formulation of *Katz et al.* (2003) where black line is their anhydrous solidus. Red line = best-fitting melt path to pressure-temperature estimates. Width of gray polygon = twice global minimum rms misfit. Projection of dotted red/gray lines to surface yields $T_p = 1390^{+85}_{-55}$ °C.

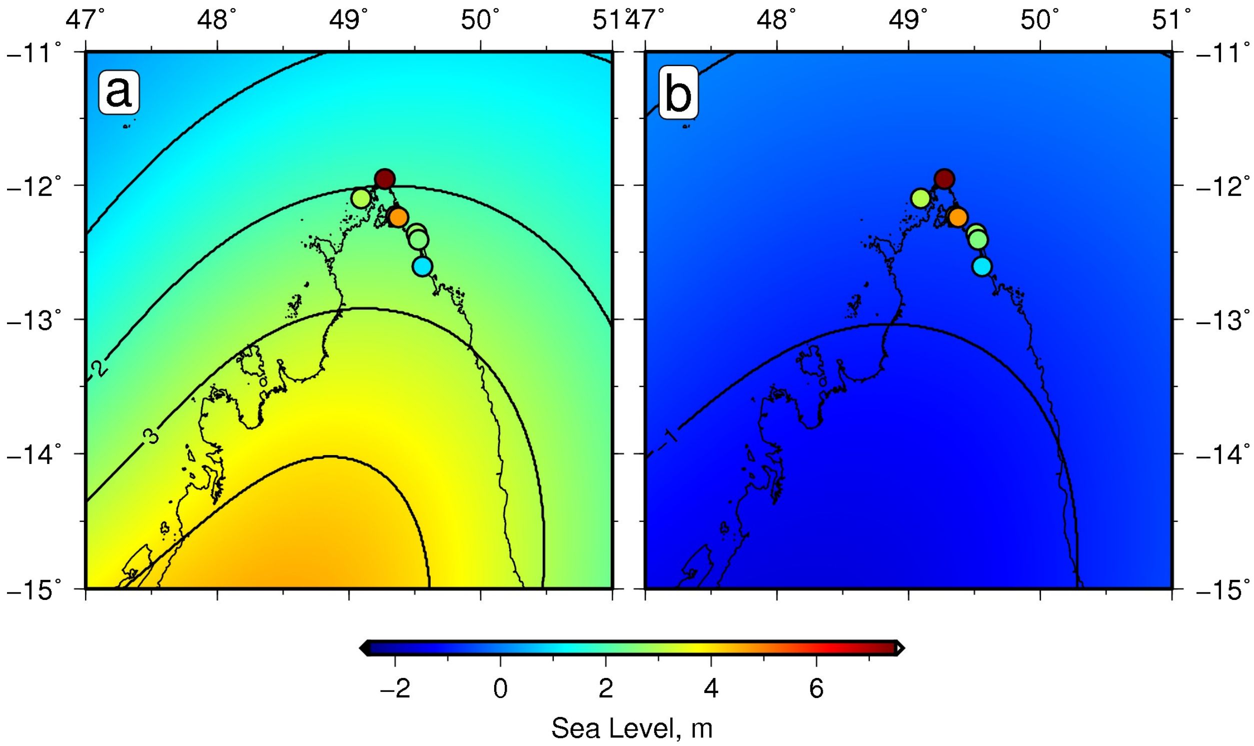

Figure 6: Glacio-isostatic models. (a) Model at start of MIS 5e, which is assumed to be 129 ka. (b) Model at end of MIS 5e, which is assumed to be 119 ka. Colored circles = sample locations as function of elevation of MIS 5e terraces.